X-Band Miniature Filters Using Lithium Niobate Acoustic Resonators and Bandwidth Widening Technique

Yansong Yang, *Graduate Student Member, IEEE,* Liuqing Gao, *Graduate Student Member, IEEE*, and Songbin Gong, *Senior Member, IEEE*

***Abstract*— This work presents a class of micro-electro-mechanical system (MEMS)-driven radio frequency filters in the X-band. The X-band center frequencies are achieved by resorting to the third-order antisymmetric Lamb wave mode (A3) in a 650-nm-thick Z-cut lithium niobate thin film. A novel bandwidth (BW) widening technique based on using the self-inductance of the top interdigital transducers and bus lines is proposed to overcome the limitations set by the electromechanical coupling (k_t^2) and satisfy the demands in miniaturization and wide BW. Four different designs of the filters are designed and fabricated to show the trade-off among BW, insertions loss (IL), out-of-band rejections, and footprint. Due to the spurious-free and high- Q performance of the A3 lithium niobate resonators, the fabricated A3 lithium niobate filters have demonstrated small in-band ripples and sharp roll-offs. One of these fabricated has demonstrated a 3-dB BW of 190 MHz, an IL of 1.5 dB, and a compact footprint of 0.56 mm^2. Another design is fabricated to demonstrate a 3-dB BW of 170 MHz, an IL of 2.5 dB, an out-of-band rejection of 28 dB, and a compact footprint of 1 mm^2.**

***Index Terms*— Acoustic filters, antisymmetric lamb waves, bandwidth (BW) widening, 5G wireless communications, Internet of things, lithium niobate, micro-electro-mechanical system (MEMS), self-inductance.**

I. Introduction

As MORE radio bands in the sub-6 GHz are licensed for 5G, the spectrum below 6 GHz is getting increasingly crowded. In addition to millimeter-wave frequencies, the systems beyond 5G should also explore higher frequencies where the propagation loss is still low, and beamforming can be avoided. However, one key challenge which lies ahead for the beyond 6-GHz systems is the lack of miniaturized front-end wideband filters [1].

The commercial solutions for the sub-6-GHz miniaturized filters are surface acoustic wave (SAW) filters and bulk acoustic wave (BAW) filters [2], [3]. For SAW devices, the operating frequencies are typically limited to be below 3.5 GHz [4], [5]. Scaling SAW devices over 3.5 GHz requires a sub-200-nm width for interdigital electrodes, which leads to high loss and poor power handling. For BAW devices, efforts have been made to scale them to the X-band (8–12 GHz) [6], [7]. To this end, AlN thin films are thinned down to be around 175 nm, which introduces very stringent requirements on film quality and thickness uniformity [8].

The lack of acoustic technologies presents the first challenge for beyond 6-GHz miniature filtering. Had any technology been scaled to beyond 6 GHz, secondary challenges remain in attaining the desired bandwidth (BW) and setting the frequency. As acoustic filters commonly use a ladder topology, the maximum BW is determined by the offset between the resonator series and antiresonance, as well as the attainable offset between the series and shunt resonators in the ladder. Thus, large fractional BW (FBW) requires not only great electromechanical coupling (k_t^2) but also the capabilities of having different frequency resonators monolithically.

One promising candidate for enabling the beyond 6-GHz miniature filters is the recently emerged antisymmetric Lamb wave devices in lithium niobate ($LiNbO_3$). The center frequency of these devices has been successfully scaled up to 60 GHz with record-breaking quality factors (Qs) by exploiting higher order modes [9]–[11]. Despite allowing the film thickness to remain unchanged, frequency scaling via increasing mode order sacrifices k_t^2. Consequently, frequency scaling comes at the expense of the reduced FBW. Moreover, the resonance of the A-mode is not as susceptible to the lateral feature size as other Lamb wave modes [12]–[15]. Thus, two resonators with frequencies separated by the target large FBW are not readily attainable. For these two reasons, the acoustic-only filters constructed on the higher order A-mode so far have limited FBW [16], [17].

In this work, we aim to address these remaining challenges and demonstrate a class of X-band wideband acoustic filters. Our approach is multi-pronged. Principally, it involves first adopting a hybrid filter topology that combines passive elements with acoustic resonators to compensate for the low k_t^2 and widen the small FBW [18]–[21]. In contrast to previous work using this principle, our approach does not use large external inductors but synergistically takes advantage of the self-inductance in the on-chip electrodes and bus lines.

Manuscript received October 15, 2020; accepted November 24, 2020. Date of publication January 27, 2021; date of current version March 4, 2021. This work was supported by the U.S. Defense Advanced Research Projects Agency—-Microsystem Technology Office (DARPA-MTO) Near Zero Power RF and Sensor Operations (NZERO) Program. *(Corresponding author: Yansong Yang.)*

The authors are with the Department of Electrical and Computing Engineering, University of Illinois at Urbana-Champaign, Urbana, IL 61801 USA (e-mail: yyang165@illinois.edu).

Color versions of one or more figures in this article are available at https://doi.org/10.1109/TMTT.2021.3049434.

Digital Object Identifier 10.1109/TMTT.2021.3049434

Then, we use a fine-controlled regional thinning technique to produce frequency offset matching the BW attained via the above *BW widening technique*.

Four different prototypes are fabricated to validate our BW widening technique and show the trade-off among FBW, insertion loss (IL), out-of-band rejection, and footprint. Among them, three designs have shown a footprint of 0.56 mm^2 with spurious-free responses and group delay variations of 5 ns. The 3-dB BW of these designs ranges from 190 MHz (FBW = 2.4%) to 380 MHz (4.4%), and the minimum IL ranges from 1.5 to 2.8 dB. A fourth design has been demonstrated in a compact footprint of 1 mm^2 with a 3-dB BW of 170 MHz (FBW = 2%), a minimum IL of 2.5 dB, and an enhanced out-of-band rejection of 28 dB. The FBWs of these prototypes have surpassed the FBW limit (1.8%) set by k_t^2 (3.6%) for an acoustic-only filter.

This article is an extension of [1], and the new material is organized as follows. Section II discusses several design aspects of the A3 $LiNbO_3$ resonators, including A3 dispersion, frequency offset, compensation of k_t^2, and static capacitance density. Section III introduces the practical considerations for A3 $LiNbO_3$ filters, including filter topology and effects from the electromagnetic (EM) and acoustic domains. Section IV presents the fabrication process and measurements of four filter designs based on the proposed BW widening technique. Section IV also discusses the spurious modes and the trade-off among BW, IL, out-of-band rejections, and footprint. Finally, Section V offers a conclusion.

II. A3 Mode $LiNbO_3$ Resonators

In this section, we will show the considerations and solutions to address the first three challenges. To achieve a center frequency beyond 6 GHz, we resort to the third-order antisymmetric Lamb wave mode (A3) resonator in a 650-nm-thick Z-cut $LiNbO_3$ thin film. Regional thinning of $LiNbO_3$ is used to achieve a wide monolithic frequency-setting range. To circumvent the limitations set by k_t^2, inductors are integrated with acoustic resonators.

A. Third-Order Antisymmetric Lamb Wave Resonator

Fig. 1(a) gives the eigen displacement mode shape of the third-order antisymmetric Lamb wave (A3). Its resonant frequency can be determined by [22]

$$f_{A3} = \frac{v_L}{2t}\sqrt{(3\alpha)^2 + \left(2\frac{t}{\lambda_L}\right)^2} \tag{1}$$

where v_L is the longitudinal acoustic velocity, t is the thickness of the plate, α is the ratio between the velocities along with the vertical and longitudinal directions, and λ_L is the longitudinal wavelength.

As C_{15} (3.69 C/m^2) in the coupling matrix of the Z-cut $LiNbO_3$ features the largest value, the lateral electric field generated by the top-only interdigital transducers (IDTs) can efficiently excite the A3 mode. Fig. 1(b) gives the cross-sectional mock-up of a $LiNbO_3$ resonator with a single pair of IDT and the corresponding simulated displacement mode shape. Due to the significant acoustic impedance mismatching, the acoustic

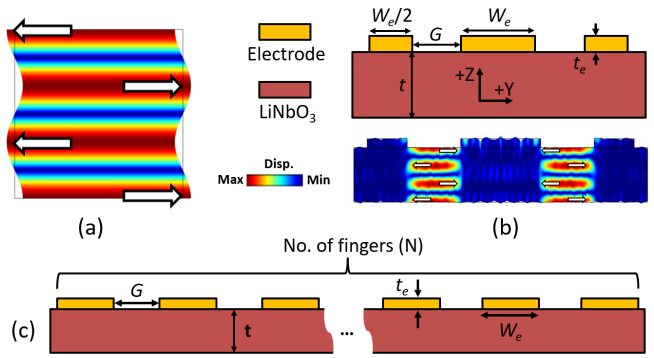

Fig. 1. (a) Displacement mode shape of the third-order antisymmetric Lamb wave mode (A3). Cross-sectional mock-up of the A3 Z-cut $LiNbO_3$ resonator (b) with three electrodes and the corresponding displacement mode shape (the arrows denote the displacement directions), (c) with multi-pair IDTs.

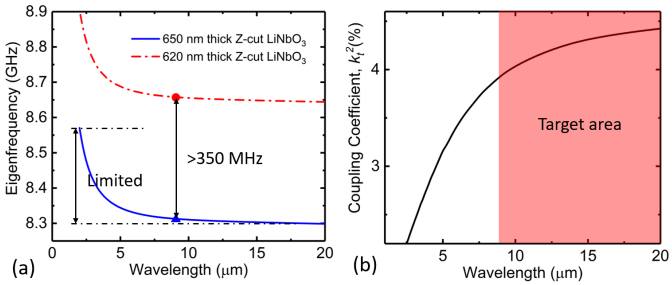

Fig. 2. (a) Dispersion curves of A3 in the 650- and 620-nm thick Z-cut $LiNbO_3$ thin films. (b) Electromechanical coupling coefficient (k_t^2) of A3 vs. the wavelength.

energy is predominantly confined between adjacent electrodes, so the longitudinal wavelength of the A3 mode is determined by the electrode separation ($G \approx \lambda_L/2$). To achieve an X-band A3 resonance, this work uses a Z-cut $LiNbO_3$ thin film of 650-nm thickness, and all the following simulations and fabrication are based on such configuration.

In filtering applications, resonator arrays based on multiple small resonators or single resonator with multiple pairs of IDTs are needed to properly match the system impedance of 50 Ω [Fig. 1(c)]. In Section IV, both the designs are presented.

B. Frequency Offset and k_t^2

The frequency offset between the series and shunt resonators in the constructed filter determines the BW. According to (1), the frequency offset can be achieved using different λ_L and lateral feature sizes (G). Due to in-house lithography limitations, G has to be larger than 1 μm for experimental validation. Based on (1), α is much larger than t/λ_L. Consequently, the frequency offset achieved through tuning the lateral feature size is limited [Fig. 2(a)]. In addition, the lateral feature size also affects k_t^2. k_t^2 as a function of λ_L is analyzed using Comsol-based finite element analysis (FEA). As shown in Fig. 2(b), a larger λ_L leads to a larger k_t^2 when λ_L is less than 8 μm, beyond which k_t^2 tends to be constant. Thus, λ_L should be over 8 μm to maximize k_t^2. However, the required

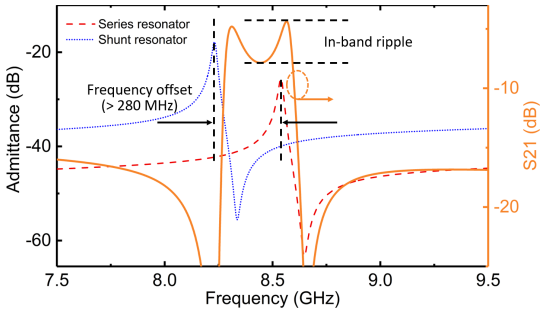

Fig. 3. Simulated admittance of the series and shunt resonators, and S21 of the constructed filter.

large value of λ_L, in turn, further limits the frequency offset [Fig. 2(a)] and leads to a larger footprint.

One method to achieve a large frequency offset and maximum k_t^2 simultaneously is to adjust the thickness of the $LiNbO_3$ thin film to set the resonance frequency. As shown in Fig. 2(a), a 30-nm thickness difference could lead to an over 350-MHz frequency offset. In this work, both the series and shunt resonators have λ_L of 8 μm but with different $LiNbO_3$ thicknesses to balance the demand for large k_t^2 and small footprint. The required thickness will be covered in Section III on filter implementation. The regional thinning process will be presented in Section IV.

C. k_t^2 Compensation and Static Capacitance Density

In addition to the frequency offset, compensation of k_t^2 should be considered as it can increase the maximum FBW. To achieve a flat in-band response, the resonant frequency of the series resonators should be close to the antiresonance of the shunt resonators. However, k_t^2 of the A3 mode excited in the Z-cut $LiNbO_3$ is around 3.6%, yielding a maximum allowed frequency offset of less than 140 MHz and a maximum filter FBW of less than 1.8%. As shown in Fig. 3, the frequency offset between the series and shunt resonator is over two times the maximum allowed value leading to a big ripple in the filter passband.

One approach to circumvent the limitation set by k_t^2 is to integrate inductors in parallel to shift the anti-resonance of the shunt resonator closer to the resonance of the series resonator [Fig. 4(a)], and another method is to integrate inductors in series to shift the resonance of the series resonator closer to the anti-resonance of the shunt resonator [Fig. 4(b)]. The equivalent circuit model (named the MBVD model) of the resonator, in which the static capacitance is captured by C_0, is shown in the inset of Fig. 4. As the directions of arrows shown in Fig. 4, the paralleled inductor leads to a smaller equivalent static capacitance, while the inductor in series helps increase the equivalent static capacitance. In other words, the series inductors contribute to higher static capacitance density leading to a smaller footprint, which will be applied in this work. The amount of footprint reduction will be discussed in Sections III and IV.

III. A3 Mode Filters Implementation

In this section, A3 mode filter designs are first discussed. To achieve better integration between the series inductors and acoustic resonators, the self-inductance of the top IDTs and bus lines is carefully modeled and used as integrated inductors in series with the acoustic resonator, thus moving the resonance and anti-resonance further apart and widening the BW of the constructed filters. Four designs of A3 mode filters are given for the implementation of X-band wideband filters.

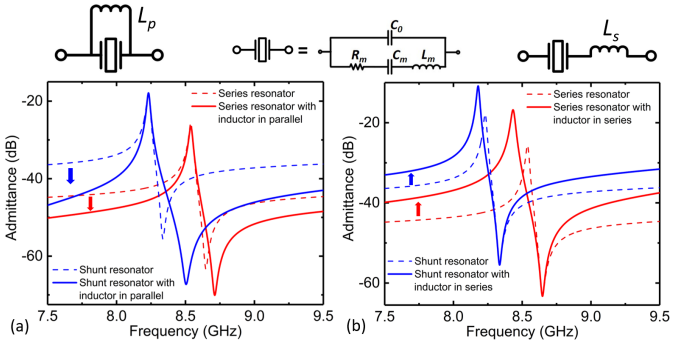

Fig. 4. Simulated admittance of the series and shunt resonators, (a) each with and without an inductor in parallel and (b) each with the without an inductor in series.

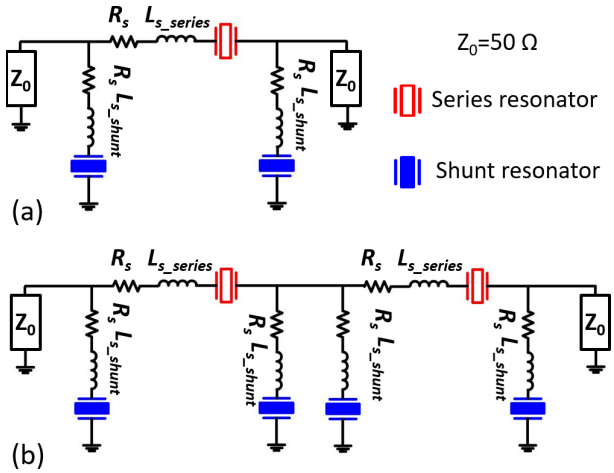

Fig. 5. (a) Ladder filter topology using one series and two shunt resonator branches. (b) Ladder filter topology using two series and four shunt resonator branches. (Both are with equivalent circuit model accounting for the EM effects.)

A. Filter Topology Structures

Two simple structures based on ladder topology using identical series and shunt resonator branches but with different filter orders are constructed (Fig. 5). L_{s_series} and L_{s_shunt} represent the inductors in series with the series and shunt resonators, respectively. The surface resistance of IDTs and bus lines is captured by including R_s in series. These two filter structures are expected to show a trade-off among IL, out-of-band rejection, and footprint. To match the system impedance of 50 Ω at the target frequency, the required static capacitance of the series (C_{series}) and shunt (C_{shunt}) resonator branches (including the series inductors) is around 230 and 450 fF, respectively.

To achieve a small footprint and sufficient k_t^2 compensation, the relationships among the static capacitance of filter

TABLE I
DESIGN PARAMETERS OF THE A3 MODE FILTERS

Design	Branch	t (nm)	W_e (μm)	G (μm)	L (μm)	t_e (nm)	t_L (nm)	No. of branches	C_0 (fF)	L_s (nH)
Design A	Series	620	6	4	110	200	400	1	120	1.6 nH
	Shunt	650	6	4	110			2	240	0.7 nH
Design B	Series	630	3	4	34			1	120	1.6 nH
	Shunt	650	3	4	34			2	240	0.7 nH
Design C	Series	612	3	4	34			1	120	1.6 nH
	Shunt	650	3	4	34			2	240	0.7 nH
Design D	Series	630	3	4	34			2	120	1.6 nH
	Shunt	650	3	4	34			4	240	0.7 nH
Conventional	Series	650	6	3	110			1	120	-
	Shunt	650	6	8	110			2	240	-

*The parameters are marked in Fig. 1

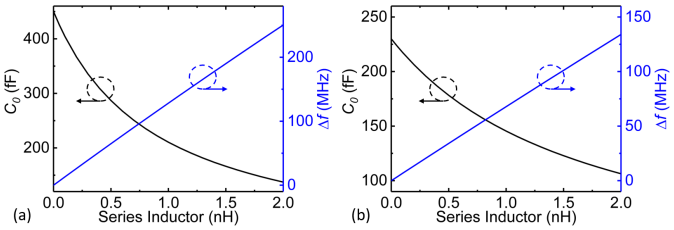

Fig. 6. Calculated relationships among C_0 of the resonator, the frequency shift of the resonance, and the series inductance for the (a) shunt branches and (b) series branches.

branches, C_0 of resonators, the frequency shift of the resonance (Δf), and the series inductance are calculated separately for the series and shunt branches. As shown in Fig. 6(a), to halve the footprint of the shunt resonators in the shunt branches, L_{s_shunt} is chosen to be 0.7 nH. Based on the above-mentioned analysis, the inductor (L_{s_series}) in series with the series resonator should be large enough to make the resonance of the series resonator closer to the anti-resonance of the shunt resonator. According to Fig. 6(b), L_{s_series} is chosen to be 1.6 nH to give Δf of 100 MHz and feature a reasonable footprint. In addition, the required C_0 of the series resonator is decreased from 230 to 120 fF.

After finalizing the static capacitance and series inductance of the series and shunt resonator branches, four different devices based on different frequency offsets (via different thicknesses of the lithium niobate thin film) are designed to show the trade-off among BW, IL, out-of-band rejection, in-band ripples, and footprint. Table I lists the design parameters of these devices, where t, W_e, G, and t_e are marked and defined in Fig. 1(b) and (c), L is the length of the resonator cavity, and t_L is the thickness of the bus lines. Designs A, B, and C resort to the ladder filter topology shown in Fig. 5(a), while Design D resorts to the ladder filter topology shown in Fig. 5(b) to enhance the out-of-band rejections. In Design A, each filter branch consists of multiple small resonators to attain a sufficient C_0. In Designs B and C, a single resonator with multiple-pair IDTs is used in each filter branch. Designs B and C resort to the same filter layout with different frequency offsets between the series and shunt resonators to verify the value of the designed series inductors. Additionally, as a comparison to the regional thinning, a conventional design resorting to varying the distance between interdigital electrodes (G) to achieve the frequency offset is also added in Table I. To fulfill Designs A, B, C, and D, the last but foremost step is to integrate inductors and acoustic resonators efficiently in a compact footprint.

Unlike previous reports [19]–[21], this work exploits the IDTs and bus lines, which are typically deemed electrically small and nonreactive at low frequency, to produce self-inductances. The inductances are then used to achieve excellent frequency shift and BW widening effects without auxiliary components. According to our previous study [9], [23], the EM effects associated with IDTs and bus lines in the filter layouts are significant beyond 6 GHz. They can be controlled by tuning the dimensions of IDTs and bus lines, including width, length, and metal thickness.

B. Hybrid Simulation

A hybrid simulation method is used to couple the effects in the EM and acoustic domains [24]. The acoustic performance is simulated with COMSOL-based FEA and captured by motional elements (R_m, L_m, and C_m) in the MBVD model (Fig. 4). The EM performance of each layout is simulated in HFSS to attain sufficient self-inductances. Internal ports are assigned in HFSS simulations for representing the layout's EM effect in the hybrid simulation. To simplify our demonstration, in each design, the series and shunt resonators use the same IDT structure with different $LiNbO_3$ thicknesses. Based on the parameters listed in Table I, the bus lines are designed to satisfy the required self-inductance (L_{s_series} and L_{s_shunt}) and shift the resonant frequencies. The filter layouts in EM simulation for Designs A, B, and C are shown in Fig. 7. Design A and the conventional design use similar filter layouts with different resonators. As shown in Fig. 8(a), the simulated response of Design A features four times larger BW than the conventional design by exploiting the self-inductance of the filter layout. Designs B and C use the same filter layout with thinner thicknesses in $LiNbO_3$ for series resonators. As shown

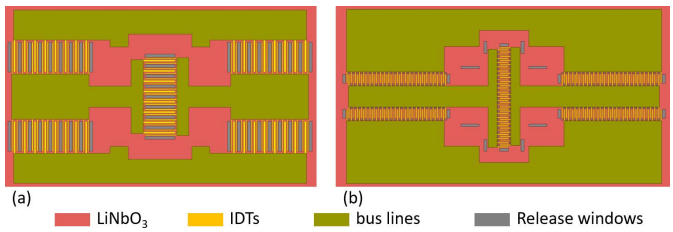

Fig. 7. HFSS EM models of the filter layouts for (a) Design A and (b) Designs B and C.

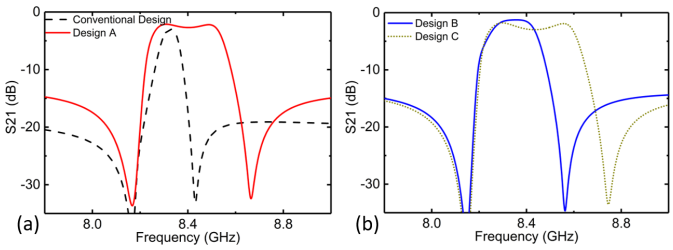

Fig. 8. Hybrid simulation results of (a) Design A and the conventional design and (b) Designs B and C.

in Fig. 8(b), Design C features a greater BW due to the larger frequency offset between the series and shunt resonators. However, a substantial ripple appears in the simulated passband of Design C as L_{s_series} is not sufficient to shift the resonance of the series resonators close to the anti-resonance of the shunt resonators. The simulations verify that the filter layout with the designed self-inductance can increase the BW and achieve a flat in-band response. As the simulation process of Design D is similar, its details are discussed later along with its measured responses.

It is worth noting that the self-inductance does not introduce extra electric loss (R_s) as IDTs and bus lines are necessities in acoustic filters. In other words, the widening of the BW of filters does not degrade IL and roll-off, nor it requires a larger footprint. Details of the filter layouts are shown in the microscope and SEM images of the fabricated devices in Section IV.

IV. Experimental Results and Discussions

A. Fabrication of A-Mode Resonators

To further demonstrate our novel approach, the filter was fabricated on a 650-nm-thick Z-cut $LiNbO_3$ thin film following the process shown in Fig. 9. After a 650-nm-thick Z-cut $LiNbO_3$ thin film is transferred onto a high-resistivity Si wafer, the release windows are defined by etching through $LiNbO_3$. In step 3, the 650-nm $LiNbO_3$ thin film is regionally thinned down to different thicknesses with a Cl_2-BCl_3-based RIE-ICP system. In step 4, the 200-nm-thick aluminum is defined as IDTs and bus lines. In the last step, XeF_2-based dry etching is used to remove the Si underneath and suspend the devices.

The $LiNbO_3$ thinning outcome is depicted in the optical microscope images. The region for the shunt resonators, where the thickness of $LiNbO_3$ is 650 nm, is shown in Fig. 10(a). The thinned region for the series resonators is shown in Fig. 10(b)

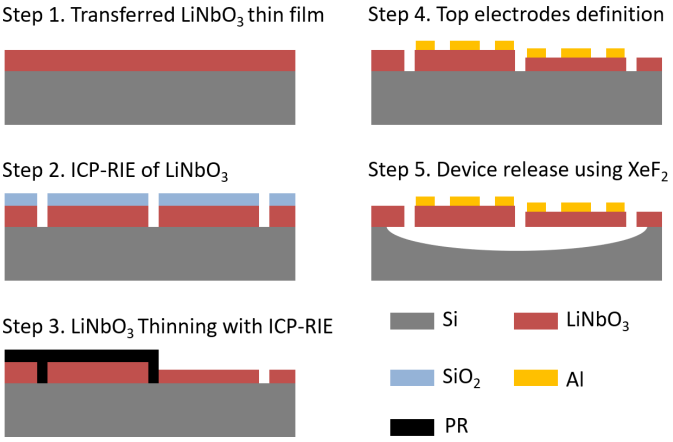

Fig. 9. Fabrication process of the A3 $LiNbO_3$ filters.

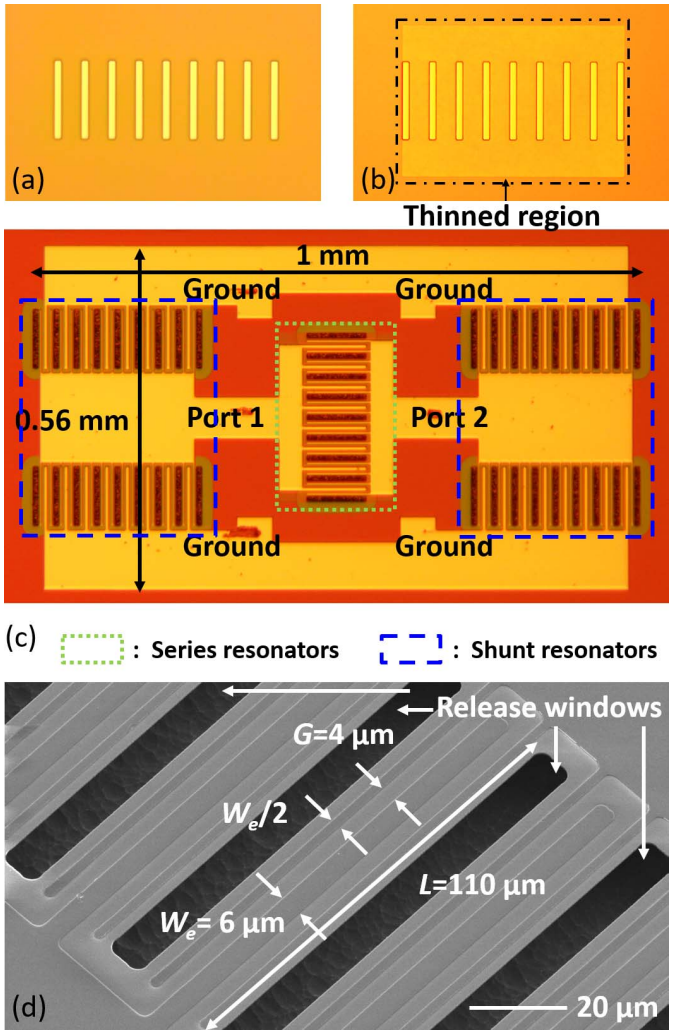

Fig. 10. Optical microscope and SEM images of Design A. (a) Region for shunt resonators. (b) Thinned region for series resonators. (c) Fabricated A3 mode $LiNbO_3$ filter. (d) Zoomed-in view of the resonator array.

for comparison. The boundary between the thinned and intact regions is clear as regions of different thicknesses present different colors under optical microscope. Fig. 10(c) shows the optical microscope images of the fabricated filter based

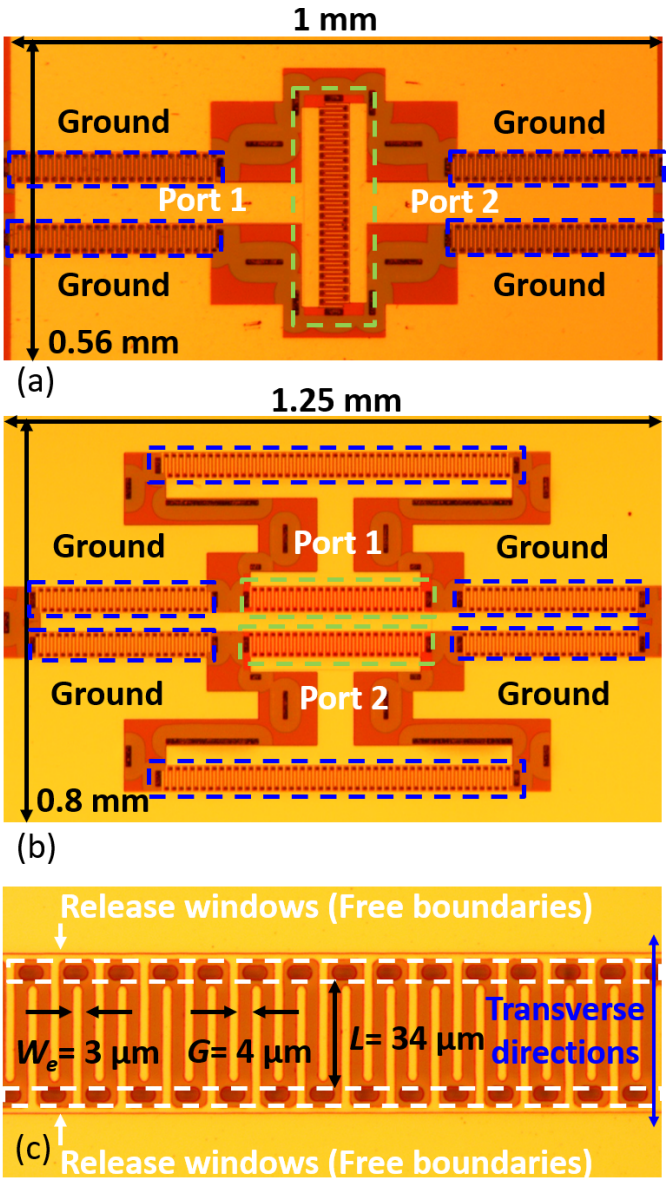

Fig. 11. Optical microscope images of (a) Designs B and C, (b) Design D, and (c) zoomed-in view of the series resonator.

on Design A. The area outlined by the green dashed lines has been thinned down to 620 nm for the series resonator array. The overall footprint of the fabricated Design A is 0.56 mm^2. The electrode separation, IDT width, and resonator cavity length are labeled in Fig. 10(d). The microscope images of the fabricated Designs B, C, and D are shown in Fig. 11. Similar to Design A, the series resonators are outlined by the green dashed lines, and the shunt resonators are labeled by the blue dashed lines. The zoomed-in view of the IDT in Designs B, C, and D is shown in Fig. 11(c). Different from Design A, the release windows are added at the transverse ends of the resonator body, acting as the free boundaries, to suppress the transverse spurious modes and achieve better acoustic energy confinement. Additionally, extra release windows are added between bus lines to generate air gaps and reduce parasitic capacitances. These fabricated filters and standalone resonators were measured with a probe station and a Keysight

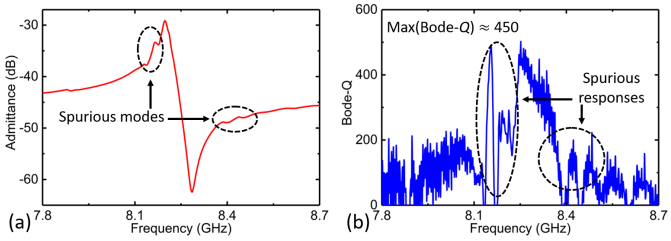

Fig. 12. (a) Measured response of the A3 $LiNbO_3$ resonator. (c) Measured Bode-Q.

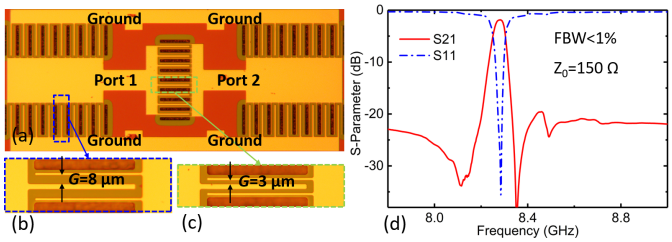

Fig. 13. Optical microscope images of the (a) fabricated A3 $LiNbO_3$ filter without regional thinning, (b) shunt resonator with G of 8 μm, and (c) series resonator with G of 3 μm. (d) Measured performance of the fabricated filter with limited BW.

N5249A PNA. The reference planes were fixed at probing pads using an SLOT chip-scale calibration kit.

B. Resonator Response

The fabricated standalone A3 $LiNbO_3$ resonator is first measured. Consistent with our theoretical analyses, the admittance response shown in Fig. 12(a) exhibits resonant frequency around 8.2 GHz with a k_t^2 of 3.6%. As seen in Fig. 12(b), the measured Bode-Q of the A3 $LiNbO_3$ resonator has a max value over 450. Several minor spurious modes exist near the resonance and anti-resonance. However, these spurious modes feature small figures of merit (FoM $= Q \cdot k_t^2$) and do not generate significant ripples.

C. Filter Responses

The conventional design resorting to varying G and hence λ_L to achieve the frequency offset [9] is fabricated as a baseline comparison to Designs A, B, C, and D [Fig. 13(a)]. In the conventional design, G for the series and shunt resonators is chosen as 3 and 8 μm, respectively, [Fig. 13(b) and (c)]. As the dispersion curve shown in Fig. 2(a), the frequency offset between the series and shunt resonators is less than 80 MHz, leading to an FBW of less than 1%. Additionally, as the impedance matching network is required to match a narrower BW, the designed static capacitances of the series and shunt resonators are insufficient to match 50 Ω. Thus, the conventional design is measured with a system impedance of 150 Ω [Fig. 13(d)].

Design A is fabricated in a similar filter layout as the conventional design. As mentioned above, the 30-nm thickness difference in the $LiNbO_3$ thin film between the series and shunt resonators leads to around 350-MHz frequency offset,

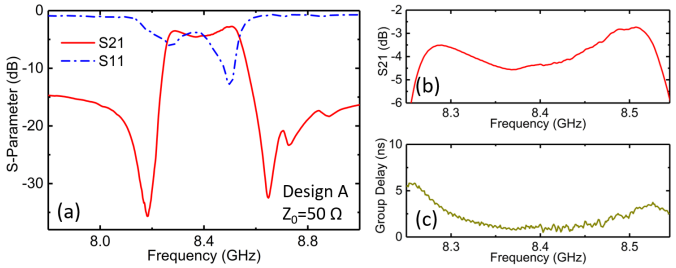

Fig. 14. (a) Measured performance of Design A. (b) Zoomed-in passband. (c) In-band group delay. All responses are measured with 50-Ω terminations.

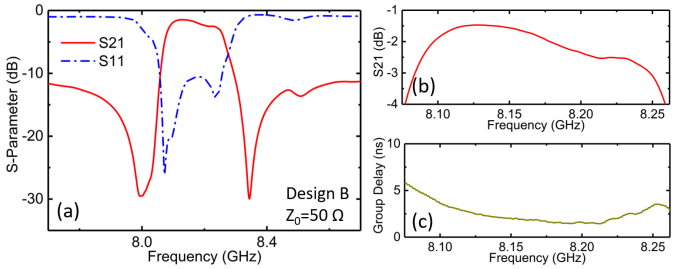

Fig. 15. (a) Measured performance of Design B. (b) Zoomed-in passband. (c) In-band group delay. All responses are measured with 50-Ω terminations.

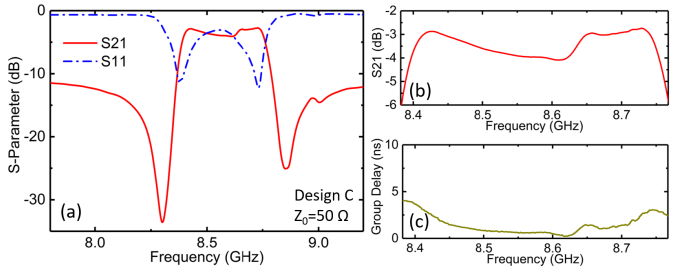

Fig. 16. (a) Measured performance of Design C. (b) Zoomed-in passband. (c) In-band group delay. All responses are measured with 50-Ω terminations.

which is four times greater than the conventional design. Due to the wide passband and the static capacitance compensation from self-inductance, Design A can match 50 Ω in a compact footprint of 0.56 mm^2. The fabricated Design A shows a center frequency of 8.4 GHz, a 3-dB FBW of 3.45% (BW = 290 MHz), a minimum IL of 2.7 dB, and an out-of-band rejection of 15 dB (Fig. 14).

Design B is fabricated in a similar size of the footprint as Design A. The main difference between Designs A and B is the structures of resonators and the frequency offset. The release windows are added in the transverse directions of the resonator body for better energy confinement and transverse spurious mode suppression. The 20-nm regional thinning makes Design B feature a 3-dB FBW of 2.4%, a minimum IL of 1.5 dB, and an out-of-band rejection of 11 dB (Fig. 15).

Design C has the same filter layout and resonator structure as Design B. The only difference between B and C is that the thickness difference in the $LiNbO_3$ thin film between the series and shunt resonators is increased to 38 nm to achieve a

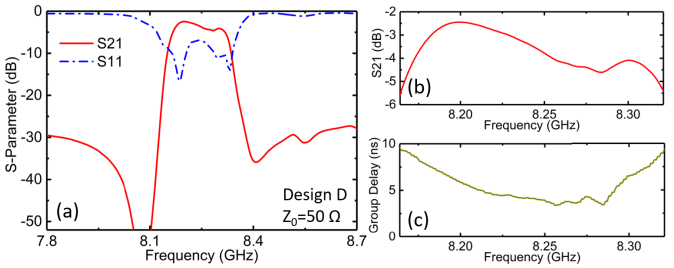

Fig. 17. (a) Measured performance of Design D. (b) Zoomed-in passband. (c) In-band group delay. All responses are measured with 50-Ω terminations.

TABLE II
COMPARISON TO THE STATE-OF-THE-ART X-BAND FILTERS

Ref.	IL (dB)	OoB Rejection (dB)	FBW	Roll-off (dB/MHz)	Footprint (mm^2)
[6]	1.7	21	3.1%	~0.23	~0.1
[7]	8.5	17	1.8%	~0.3	~0.1
[25]	3.8	25	4%	0.062	1680
[26]	0.6	26	10%	~0.2	>3400
Design A	2.7	15	3.45%	0.39	0.56
Design B	1.5	11	2.4%	0.46	0.56
Design C	2.8	11	4.42%	0.35	0.56
Design D	2.5	28	2%	0.74	1

large frequency offset of over 400 MHz. Due to the large frequency offset, Design C shows a 3-dB FBW of 4.42% with a minimum IL of 2.8 dB (Fig. 16). Consistent with the above analyses, the self-inductances of the filter layout are insufficient to compensate for the lack of k_t^2 for such a wide passband, leading to a 1-dB ripple in the passband.

Design D is designed with a higher order topology than other designs. To include the additional resonators, the footprint of Design D is increased to 1 mm^2. As shown in Fig. 17, the fabricated Design D shows a 3-dB FBW of 2% (BW = 170 MHz), a minimum IL of 2.5 dB, and an enhanced out-of-band rejection of 28 dB.

Although the responses of all designs are smooth, the minor spurious responses still can be identified in the zoomed-in in-band responses (S21 and group delay) of Design A. In contrast, other designs have clean responses. The in-band ripples are caused by the transverse spurious modes of the resonators. The different ripple responses are from the different resonator structures in designs. It validates that the release windows in the transverse directions can mitigate the transverse spurious modes. Additionally, Designs B and D feature lower IL than Design A, which validates the better energy confinement introduced by the extra release windows. The group delay variations over the passband of all these devices are less than 5 ns [Figs. 14(c), 15(c), 16(c), and 17(c)], which is sufficiently

small to avoid RF signal distortion. The key measured parameters of the fabricated filters are listed in Table II.

Table II compares both the SOA acoustic and EM filters with our four designs. The previous reports of X-band acoustic filters are all based on BAW. Their limitations have been discussed in Section I. The SoA EM filters resort to cavities with low-loss dielectric materials [25], [26] to achieve wide BW and low IL. However, due to the orders of magnitude higher velocity of EM waves, the SoA EM filters feature a footprint of several thousand times larger. Additionally, our four designs feature sharper roll-off than SoA due to the high-Q of A3 $LiNbO_3$ resonators. Our demonstration offers a combination of enhancements over SoA, particularly for handheld applications where size and performance are important.

V. Conclusion

In this work, X-band acoustic filters based on the third-order antisymmetric mode in the Z-cut $LiNbO_3$ have been demonstrated. A novel BW widening technique that uses the self-inductance of the interdigital electrodes and bus lines has been shown to circumvent the BW limitations and satisfy the demands in miniaturization. The acoustic–EM hybrid solutions show the strong potential of LiNbO3 higher order antisymmetric mode devices for beyond 6-GHz front-ends.

References

[1] Y. Yang, L. Gao, and S. Gong, "An X-band lithium niobate acoustic RFFE filter with FBW of 3.45% and IL of 2.7 dB," in *IEEE MTT-S Int. Microw. Symp. Dig.*, Aug. 2020, pp. 249–252.

[2] *5G New Radio Solutions?: Revolutionary Applications Here Sooner Than You Think*, Skyworks Solutions, San Irvine, CA, USA. Accessed: Nov. 5, 2019. [Online]. Available: https://www.skyworksinc.com

[3] K. Hashimoto, *RF Bulk Acoustic Wave Filters for Communications*. Norwood, MA, USA: Artech House, 2009.

[4] T. Kimura, M. Omura, Y. Kishimoto, and K. Hashimoto, "Comparative study of acoustic wave devices using thin piezoelectric plates in the 3–5-GHz range," *IEEE Trans. Microw. Theory Techn.*, vol. 67, no. 3, pp. 915–921, Mar. 2019.

[5] T. Kimura *et al.*, "A high velocity and wideband SAW on a thin $LiNbO_3$ plate bonded on a Si substrate in the SHF range," in *Proc. IEEE Int. Ultrason. Symp. (IUS)*, Oct. 2019, pp. 1239–1248.

[6] M. Ueda *et al.*, "Development of an X-band filter using air-gap-type film bulk acoustic resonators," *Jpn. J. Appl. Phys.*, vol. 47, no. 5, pp. 4007–4010, May 2008.

[7] T. Matsumura, M. Esashi, H. Harada, and S. Tanaka, "Multi-band RF filter integrating different modes of AlN resonator by CMOS-compatible process," in *Proc. IEEE Int. Ultrason. Symp.*, Sep. 2009, pp. 2141–2144.

[8] R. Aigner, G. Fattinger, M. Schaefer, K. Karnati, R. Rothemund, and F. Dumont, "BAW filters for 5G bands," in *IEDM Tech. Dig.*, Dec. 2018, p. 14.

[9] Y. Yang, R. Lu, T. Manzaneque, and S. Gong, "Toward Ka band acoustics: Lithium niobate asymmetrical mode piezoelectric MEMS resonators," in *Proc. IEEE Int. Freq. Control Symp. (IFCS)*, May 2018, pp. 1–5.

[10] V. Plessky, S. Yandrapalli, P. J. Turner, L. G. Villanueva, J. Koskela, and R. B. Hammond, "5 GHz laterally-excited bulk-wave resonators (XBARs) based on thin platelets of lithium niobate," *Electron. Lett.*, vol. 55, no. 2, pp. 98–100, Jan. 2019.

[11] Y. Yang, R. Lu, L. Gao, and S. Gong, "10–60-GHz electromechanical resonators using thin-film lithium niobate," *IEEE Trans. Microw. Theory Techn.*, vol. 68, no. 12, pp. 5211–5220, Dec. 2020.

[12] S. Gong and G. Piazza, "Design and analysis of lithium–niobate-Based high electromechanical coupling RF-MEMS resonators for wideband filtering," *IEEE Trans. Microw. Theory Techn.*, vol. 61, no. 1, pp. 403–414, Jan. 2013.

[13] S. Gong and G. Piazza, "Monolithic multi-frequency wideband RF filters using two-port laterally vibrating lithium niobate MEMS resonators," *J. Microelectromech. Syst.*, vol. 23, no. 5, pp. 1188–1197, Oct. 2014.

[14] R. H. Olsson *et al.*, "A high electromechanical coupling coefficient SH0 lamb wave lithium niobate micromechanical resonator and a method for fabrication," *Sens. Actuators A, Phys.*, vol. 209, pp. 183–190, Mar. 2014.

[15] R. Wang, S. A. Bhave, and K. Bhattacharjee, "High $k_t^2 \times Q$, multi-frequency lithium niobate resonators," in *Proc. IEEE 26th Int. Conf. Micro Electro Mech. Syst. (MEMS)*, Jan. 2013, pp. 165–168.

[16] Y. Yang, R. Lu, and S. Gong, "Scaling acoustic filters towards 5G," in *IEDM Tech. Dig.*, Dec. 2018, p. 39.

[17] Y. Yang, R. Lu, A. Kourani, and S. Gong, "Advancing lithium niobate based thin film devices for 5G front-ends," in *IEEE MTT-S Int. Microw. Symp. Dig.*, Jun. 2019, pp. 881–884.

[18] O. Ikata, T. Miyashita, T. Matsuda, T. Nishihara, and Y. Satoh, "Development of low-loss band-pass filters using SAW resonators for portable telephones," in *Proc. IEEE Ultrason. Symp.*, Oct. 1992, pp. 111–115.

[19] X. Lu, K. Mouthaan, and Y. T. Soon, "Wideband bandpass filters with SAW-Filter-Like selectivity using chip SAW resonators," *IEEE Trans. Microw. Theory Techn.*, vol. 62, no. 1, pp. 28–36, Jan. 2014.

[20] D. Psychogiou, R. Gomez-Garcia, R. Loeches-Sanchez, and D. Peroulis, "Hybrid acoustic-wave-lumped-element resonators (AWLRs) for high-Q bandpass filters with quasi-elliptic frequency response," *IEEE Trans. Microw. Theory Techn.*, vol. 63, no. 7, pp. 2233–2244, Jul. 2015.

[21] C. Zuo, C. He, W. Cheng, and Z. Wang, "Hybrid filter design for 5G using IPD and acoustic technologies," in *Proc. IEEE Int. Ultrason. Symp. (IUS)*, Oct. 2019, pp. 1–4.

[22] D. Royer, D. P. Morgan, and E. Dieulesaint, *Elastic Waves in Solids I: Free and Guided Propagation*. Berlin, Germany: Springer, 2000.

[23] Y. Yang, R. Lu, L. Gao, and S. Gong, "4.5 GHz lithium niobate MEMS filters with 10% fractional bandwidth for 5G front-ends," *J. Microelectromech. Syst.*, vol. 28, no. 4, pp. 575–577, Aug. 2019.

[24] M. Chatras *et al.*, "Modeling and design of BAW resonators and filters for integration in a UMTS transmitter," in *Modeling and Measurement Methods for Acoustic Waves and for Acoustic Microdevices*, Rijeka, Croatia: InTechOpen, 2013.

[25] F. T. Ladani, S. Jam, and R. Safian, "A novel X-band bandpass filter using substrate integrated waveguide resonators," in *Proc. IEEE Asia–Pacific Conf. Appl. Electromagn. (APACE)*, Nov. 2010, pp. 1–5.

[26] D. Miek, S. Simmich, and M. Hoft, "Additive manufacturing of symmetrical X-band waveguide filters for wide-band applications based on extracted pole filter design," in *IEEE MTT-S Int. Microw. Symp. Dig.*, Jul. 2019, pp. 13–15.

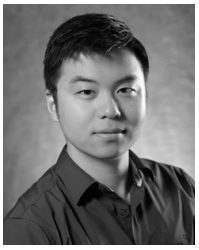

Yansong Yang (Graduate Student Member, IEEE) received the B.S. degree in electrical and electronic engineering from the Huazhong University of Science and Technology, Wuhan, China, in 2014, and the M.S. and Ph.D. degrees in electrical engineering from the University of Illinois at Urbana–Champaign, Urbana, IL, USA, in 2017 and 2019, respectively.

He is currently a Post-Doctoral Researcher with the University of Illinois at Urbana–Champaign. His research interests include design and microfabrication techniques of RF MEMS resonators, filters, switches, and photonic integrated circuits.

Dr. Yang was a recipient of the Second Place in Best Paper Competition at the 2018 IEEE International Microwave Symposium and the best paper award at 2019 IEEE International Ultrasonics Symposium. He was also a finalist for the Best Paper Award at 2018 IEEE International Frequency Control Symposium. He is also a recipient of the 2019 P. D. Coleman Graduate Research Award from the Department of Electrical and Computer Engineering at UIUC.

Liuqing Gao (Graduate Student Member, IEEE) received the B.S. and M.S. degrees in electrical engineering from the University of Illinois at Urbana–Champaign, Urbana, IL, USA, in 2016 and 2020, respectively, where she is currently pursuing the Ph.D. degree.

Her research interests include design and microfabrication techniques of MEMS resonators, filters, and wireless communication systems.

Dr. Gao was a recipient of the Best Student Paper Award at 2020 IEEE International Ultrasonics Symposium, the 3rd place in Best Paper Competition at 2020 IEEE International Microwave Symposium, the 2015 Omron Electrical Engineering Scholarship, the 2016 E. C. Jordan Awards, the 2016 Illinois Engineering Achievement Scholarship, the 2016 Highest Honors at Graduation, the 2017 ECE Distinguished Research Fellowship, the 2018 James M. Henderson Fellowship, the 2019 Dr. Ok Kyun Kim Fellowship, and the 2020 John Bardeen Graduate Research Award from the Department of Electrical and Computer Engineering at UIUC.

Songbin Gong (Senior Member, IEEE) received the Ph.D. degree in electrical engineering from the University of Virginia, Charlottesville, VA, USA, in 2010.

He is currently an Associate Professor and the Intel Alumni Fellow with the Department of Electrical and Computer Engineering and the Micro and Nanotechnology Laboratory, University of Illinois at Urbana–Champaign, Urbana, IL, USA. His research primarily focuses on design and implementation of radio frequency microsystems, components, and subsystems for reconfigurable RF front-ends. In addition, his research explores hybrid microsystems based on the integration of MEMS devices with photonics or circuits for signal processing and sensing.

Dr. Gong was a recipient of the 2014 Defense Advanced Research Projects Agency Young Faculty Award, the 2017 NASA Early Career Faculty Award, the 2019 UIUC College of Engineer Dean's Award for Excellence in Research, and 2019 Ultrasonics Early Career Investigator Award. Along with his students and postdocs, he received the Best Paper Awards from the 2017 and 2019 IEEE International Frequency Control Symposium, the 2018, 2019, and 2020 International Ultrasonics Symposium, and won second and third place in Best Paper Competition at the 2018 and 2020 IEEE International Microwave Symposium. He is a Technical Committee Member of the IEEE International Microwave Symposium, International Frequency Control Symposium, and International Ultrasonic Symposium. He currently serves as the Chair of MTT TC6 and an Associate Editor for T-UFFC, JMEMS, and JMW.